Secondary crystalline phases identification in $Cu_2ZnSnSe_4$ thin films: contributions from Raman scattering and photoluminescence

Pedro M. P. Salomé · Paulo A. Fernandes · Joaquim P. Leitão · Marta G. Sousa · Jennifer P. Teixeira · António F. da Cunha

Abstract In this work, we present the Raman peak positions of the quaternary pure selenide compound $Cu_2ZnSnSe_4$ (CZTSe) and related secondary phases that were grown and studied under the same conditions. A vast discussion about the position of the X-ray diffraction (XRD) reflections of these compounds is presented. It is known that by using XRD only, CZTSe can be identified but nothing can be said about the presence of some secondary phases. Thin films of CZTSe, Cu_2SnSe_3, ZnSe, SnSe, $SnSe_2$, $MoSe_2$ and a-Se were grown, which allowed their investigation by Raman spectroscopy (RS). Here we present all the Raman spectra of these phases and discuss the similarities with the spectra of CZTSe. The effective analysis depth for the common back-scattering geometry commonly used in RS measurements, as well as the laser penetration depth for photoluminescence (PL) were estimated for different wavelength values. The observed asymmetric PL band on a CZTSe film is compatible with the presence of CZTSe single-phase and is discussed in the scope of the fluctuating potentials' model. The estimated bandgap energy is close to the values obtained from absorption measurements. In general, the phase identification of CZTSe benefits from the contributions of RS and PL along with the XRD discussion.

P. M. P. Salomé (&)
Ångström Laboratory, Ångström Solar Center, Solid State Electronics, Uppsala University, PO Box 534, 751 21 Uppsala, Sweden
e-mail: pedrosalome@gmail.com

P. M. P. Salomé
International Iberian Nanotechnology Laboratory (INL), Laboratory for Nanostructured Solar Cells (LaNaSC), Av. Mestre José Veiga, 4715-330 Braga, Portugal

P. A. Fernandes
Departamento de Física, Instituto Superior de Engenharia do Porto, Instituto Politécnico do Porto, Rua Dr. António Bernardino de Almeida, 431, 4200-072 Porto, Portugal

J. P. Leitão · M. G. Sousa · J. P. Teixeira · A. F. da Cunha
I3N and Departamento de Física, Universidade de Aveiro, Campus Universitário de Santiago, 3810-193 Aveiro, Portugal
e-mail: joaquim.leitao@ua.pt

Introduction

$Cu_2ZnSnSe_4$ (CZTSe) is a quaternary semiconductor used as the absorber layer in thin film solar cells. Together with Cu_2ZnSnS_4 (CZTS), these materials are interesting because they replace the rare and expensive elements used in $Cu(In,Ga)Se_2$(CIGS), such as In and Ga, with inexpensive and abundant ones, Sn and Zn. The most efficient solar cell made with $Cu_2ZnSn(S,Se)_4$ (CZTSSe) was prepared by Wang et al. [1] and reached a power conversion efficiency of 12.6 %. For the single-chalcogenide materials, the records are 8.4 % for CZTS [2] and 9.7 % for CZTSe [3]. In addition to small solar cell devices, CZTS mini-modules are also being researched and an efficiency of 9.2 % was demonstrated [4]. Despite this very encouraging proof of concept, the future industrialization process still has open questions such as material and cell performance stability that need to be further investigated by the research community. In spite of this race for high values of power conversion efficiency, several growth methods are being researched for thin films [5–12] and nano-particles [13–25]. These techniques are being researched in order to find new approaches that might further increase efficiency in the future.

The mentioned efficiency values prove that these materials can be used to make solar cells but it should be noticed that most of their physical properties are still largely unknown, and a deeper understanding of the materials' properties is still needed. For this investigation, it is mandatory to grow single-phase materials and to be able to perform a correct identification of the crystalline phase. As a matter of fact, phase identification is a major problem when working with this compound. The standard technique for this purpose, X-ray diffraction (XRD), is insufficient to resolve the various phases that may form. In XRD, resolving CZTSe from unwanted secondary phases such as ZnSe is difficult because of the overlap of the main diffraction peaks. A solution for this problem is to use Raman spectroscopy (RS) complemented by photoluminescence (PL) commonly used to overcome the XRD limitation [26–31]. In this paper, we study with RS the most common secondary/unwanted phases that might appear during the growth of pure Selenide quaternary compound CZTSe which, to the best of our knowledge, is done for the first time in the same work. Thus, we avoid the constraints of comparing the results from several works in the literature obtained with different experimental conditions. The samples were prepared in a two-step approach, which is the most used technique to grow CZTSe-based devices. All samples were measured under the same conditions. In addition, we study the Raman's and PL effective analysis depth and, by PL, the electronic level structure of the CZTSe phase and the non-radiative recombination channels of single-phase layers. Together, these analyses confirm that single-phase material growth has occurred and provide insight into several important fundamental properties.

Literature review of XRD

A common way to prepare CZTSe is to anneal/selenize precursor layers and this approach is commonly described as a two-step process. During the selenization, the thermodynamic conditions, such as pressure, temperature and Se atmosphere, can be varied to such an extent that the elements in the sample will be able to form binary, ternary and quaternary phases [32–40]. Other growth methods follow similar thermodynamic conditions so they also have to deal with unwanted secondary phases [18, 41, 42]. Ideally, one wants to prepare single-phase CZTSe films but if some of those secondary phases are still present after the deposition, then the performance of the resulting solar cells may be degraded. Secondary phases may harm device performance by forming recombination centres [43, 44], areas where no photocurrent is created, (dead areas) [45] or shunt paths [46]. In Table 1, we present several structural parameters, collected from the literature, for CZTSe and different related phases that may be present during the formation process of CZTSe [41, 47–51]. CZTSe, cubic-ZnSe, cubic-Cu_2SnSe_3 (CTSe) and cubic-Cu_2Se have a very similar structure and a very similar unit cell size. Given that CZTSe has a tetragonal based structure, most of its reflections occur in the same angular position as the reflections of the above mentioned phases [52]. This is due to several reasons: (1) all structures derive from the same family, the cubic one; (2) the lattice parameters are very close, for instance when comparing the lattice parameter a of CZTSe with the ones of cubic-CTSe and cubic-ZnSe [53], differences of 0.004 and 0.02 Å are found, respectively, and (3) $Cu^{þ}$ and $Zn^{2þ}$ are neighbours in the periodic table and have a very similar atomic scattering factor [54] to which is proportional the measured intensity in an X-ray diffraction experiment. From all phases mentioned in Table 1, CuSe, SnSe and $SnSe_2$ can be resolved from CZTSe using XRD since they have quite different structures and cell parameters. There are other phases like, for instance, monoclinic CTSe [55–57], which may form during the growth of CZTSe but since they have very different crystalline structures they can be identified in XRD, however, there are not many reports that show them as secondary phases during the growth of CZTSe. By looking at Table 2 it is evident that the problem of similar structures and lattice parameters for CZTSe, ZnSe and CTSe is reflected in the small difference between the XRD peak positions. Note that on Table 2, we only show the CZTSe peaks that overlap with the selected secondary phases. It also shows the angular differences between the position of the unwanted phases and the position of CZTSe. For ZnSe, the largest difference is 0.15° and, in this case, the CZTSe peak is located at 72.48° whereas the ZnSe peak is situated at 72.63°, but the intensities of these peaks are too low for differences to be seen clearly [53]. Usual system resolutions for standard h–$2h$ measurements are close to these angular differences. With broad peaks, this distinction is even harder to be detected. For the cubic-CTSe, the biggest difference is 0.16°.

In spite of the fact that all the cubic-ZnSe and cubic-CTSe diffraction peaks are extremely close and/or superimposed with those of CZTSe, the latter possesses additional peaks that do not match with the ones from these unwanted phases. Such examples are the peaks at 15.61° and 17.42°, and the three combinations of double peaks located around 53°, 65° and 72°. Usually, the intensity of the double peaks close to 65^0 and 72^0 are low and therefore the peaks located at $53{:}39^0$ and $53{:}53^0$ can be used to evaluate the presence or absence of CZTSe [47]. Using these peaks, one can then say whether CZTSe is present. However, just based on XRD measurements, nothing can

Table 1 Structural and optical information of CZTSe and related phases

Compound	CZTSe	ZnSe	CTSe	Cu_2Se	CuSe	SnSe	$SnSe_2$
Structure	Tetragonal	Cubic	Cubic	Cubic	Hexagonal	Orthorhombic	Hexagonal
a (Å)	5.6882	5.669	5.684	5.763	3.984	4.46	3.8108
b (Å)	–	–	–	–	–	11.57	–
c (Å)	11.3378	–	–	–	17.288	4.19	6.141
Cell volume ($Å^3$)	366.8	182.17	183.64	191.4	237.64	216.21	77.23
E_{gap} (eV)	1.05 (D)	2.6 (D)	0.74–0.84 (D)	2.2 (D)	2.2 (D)	1.26 (D)	1.7 (D)
						0.90 (I)	0.92 (I)
	Refs. [61, 62]	Ref. [67]	Refs. [68–70]	Refs. [71, 72]	Ref. [71]	Ref. [73, 74]	Ref. [74, 75]

The structural information was retrieved from literature [53]. The type of the band edge structure is denoted by D and I for direct and indirect bandgap semiconductors, respectively. The references for the values of the bandgap energies are mentioned in the last line of the table

Table 2 Positions of the XRD peaks for CZTSe that might overlap with other phases: ZnSe and CTSe

CZTSe angle (^{0})	Planes	ZnSe angle (^{0})	Planes	Difference to CZTSe (^{0})	CTSe angle (^{0})	Planes	Difference to CZTSe (^{0})
27.16	112	27.22	111	-0.06	27.15	111	0.01
45.12	204	45.20	220	-0.08	45.07	220	0.05
53.39	312	–	–	–	–	–	–
53.53	116	53.57	311	-0.04	53.41	311	0.12
65.59	400	–	–	–	–	–	–
65.84	008	65.84	400	0.00	65.64	440	0.20
72.36	332	–	–	–	–	–	–
72.48	316	72.63	331	-0.15	72.41	331	0.07
83.19	424	–	–	–	–	–	–
83.35	406	83.46	422	-0.11	83.19	422	0.16

The angular values are estimated for a X-ray incident wavelength of 1.54060 Å and were measured for powder reference samples. The angular differences with respect to the CZTSe-related reflections [53] are presented

be said regarding the presence of the other two phases. If the unique peaks of CZTSe are not present, then one cannot immediately say that CZTSe is not present because the crystalline quality of the material could be poor which would cause a broadening of the diffraction peaks.

Some literature uses only XRD to evaluate the presence of secondary phases, and so the authors believe that some of the presented properties, supposedly belonging to CZTSe, may be, in reality, related to unwanted phases. Such an example is the bandgap energy, for which reported values ranging from 1.0 to 1.5 eV are found in the literature [58–60]. This property of CZTSe was the object of a debate for some time until Salomé et al. and Ahn et al. have confirmed the bandgap energy to be 1.05 eV [61–63], by analysing the absorption coefficient and by performing PL measurements. As a reference, the bandgap energies for CZTSe and other secondary phases are presented in Table 1. Until the optimal growth conditions are established, one needs to have as much information as possible on how to identify these unwanted phases. A solution would be to perform very detailed h–$2h$ measurements and to perform Rietveld analyses [64–66] in order to deconvolute the superimposed peaks, however, this kind of analysis is complex to perform. A possible way is the use of RS complemented by PL.

Experimental section

All samples studied in this work were prepared using a growth method based on selenization of metallic precursors described in detail elsewhere [73]. The precursors were deposited using DC-magnetron sputtering on soda lime glass (SLG) [47, 74, 76], and the selenization pressures and temperatures were tuned for each compound according to our own experience and the literature data presented in Table 1. Mo, Cu, Zn and Sn metallic precursors were sputtered from targets with purity of 3N for Mo, 5N for Cu and 4N for Zn and Sn. Mo is the metal used for back contact in standard thin film solar cells [77]. The deposition was done at room temperature with a substrate-to-sample distance of 10 cm, with a power density of 0.16 Wcm^{-2} and a working pressure of 2×10^{-3} mbar. The thicknesses and deposition rates were monitored using a quartz crystal

Intellemetrics IL 150. The selenization was done in a separate chamber with a base pressure of 1×10^{-5} mbar. Se was evaporated at 250 ^{0}C. CZTSe, $Cu_{2-x}Se$, $MoSe_2$ and CTSe were prepared at 540 ^{0}C and 1 mbar. ZnSe was formed at 350 ^{0}C and 1 mbar. SnSe was formed at 570 ^{0}C and 500 mbar, $SnSe_2$ at 300 ^{0}C and 600 mbar, a-Se at 470 ^{0}C and 600 mbar. Se_8 was formed by heating a glass substrate coated with graphene to 530 ^{0}C and exposed to Se vapours under vacuum, more details on this growth method will be published elsewhere. Argon was used to increase the pressure from the chambers' base pressure to the growth pressure of the compounds. The films had a thickness between 500 and 1500 nm. Chemical composition of the precursors was analysed using an ICP-MS Thermo X Series. The crystalline structure was studied by the XRD with a PHILIPS PW 3710 diffractometer using the Cu-K_a line (1.54060 Å). RS was performed using a Jobin-Yvon T64000 RS system with an Olympus microscope equipped with a 100x magnification lens in the back-scattering configuration. The excitation source was an $Ar^þ$ ion laser operating at the wavelength of 488 nm, with excitation power of 1–5 mW and spot diameter of """ 0.7 lm. RS measurements were made in room temperature conditions without intentional cooling or heating. The PL measurements were carried out using a Bruker IFS 66v Fourier transform infrared (FTIR) spectrometer equipped with a Ge diode detector cooled at the liquid nitrogen temperature. The samples were inserted in a nitrogen gas flow cryostat which allowed the change in temperature in the range 70–300 K. The excitation source was a 514.5 nm laser line focused on the sample in a spot of """ 200 lm diameter. The power of the laser was measured at the front of the cryostat window. For PL measurements, the samples were grown on Mo-coated SLG, which was done in order to make the measurements on CZTSe with the same properties as the CZTSe that is used for solar cells.

Results and discussion

Raman scattering

The use of RS for phase identification requires reference samples and for that it is needed to grow single-phase samples that allow the correct identification of their Raman peaks. In this work, we perform a comprehensive RS investigation of the most common secondary phases that could be present during the growth of CZTSe. In Fig. 1, we present RS spectra for several phases: CZTSe, CTSe, ZnSe, SnSe, $SnSe_2$, a-Se, $MoSe_2$. For the $Cu_{2-x}Se$ phase, no spectrum is presented due to the fact that with different x contents the main peak shifts from 260 to 270 cm^{-1} and growing phases with different x values is complex [71, 72]. The assignment of the peaks to each phase was confirmed through a bibliographical survey, as shown in Table 3, and the identification of the phases was obtained after the comparison with XRD measurements for all samples. According to the analyses, all studied compounds are single-phase and the only compound where there might be a secondary phase is amorphous Se (a-Se), since there is a broad peak located at 237 cm^{-1} which could be associated with trigonal Se_8 [78]. We grew the most likely secondary phases that might appear during the growth of CZTSe, but, in addition to all phases presented in Table 3, there is the possibility that other Se-related phases, stable at room temperature, could be formed. Such phases are monoclinic CTSe, hexagonal Se_n, *a*-monoclinic Se_8, *c*-monoclinic Se_8, rhombohedric Se_6, among others [78]. None of these phases were ever detected in our various deposition conditions or ever reported in the literature as secondary phases of CZTSe. Consequently, we have not considered them in our analysis.

A careful analysis of Table 3 shows that with RS, one can always tell if CZTSe is present since it has three very well distinguishable peaks at 174 (A symmetry), 195 (A symmetry), 233 cm^{-1} (B symmetry) [88–90], as seen in that Table and Fig. 1a. Using peak fit methodology, one should be able to find more peaks in the RS spectra of CZTSe, but for the main purpose of this work, phase identification, such step is not necessary. At this point, it is worth mentioning that, for the CZTS system, it is quite hard to distinguish CZTS from ZnS for two reasons: (1) the main Raman peaks of both compounds are quite close [91, 92]; (2) ultra-violet light is required as the excitation wavelength in order to create resonant conditions [27]. On the other hand, in the case of ZnSe, its Raman signal is strong and the main ZnSe peak is located at 250 cm^{-1} which is quite distant than the CZTSe's peaks, making the identification possible. Several publications have showed the appearance of ZnSe along with the CZTSe peaks [47, 93]. This shows that this technique is more useful for the identification of secondary phases in CZTSe than in CZTS.

A phase that might be difficult to identify is cubic-CTSe, since the XRD peaks overlap with some of the peaks of CZTSe, and in Raman its main peak is found at 180 cm^{-1}, right between the two main peaks of CZTSe, 174 and 195 cm^{-1}. The identification of CTSe will depend on the crystalline quality which is reflected on the full width at half maximum of the peaks and in the relative amounts of the two phases. With the exception of CTSe, all of the other phases shown here, when present in a solid mixture with CZTSe, should be resolved by RS.

We must note that values presented in Table 3 are the ones measured in this work. The establishment of a clear

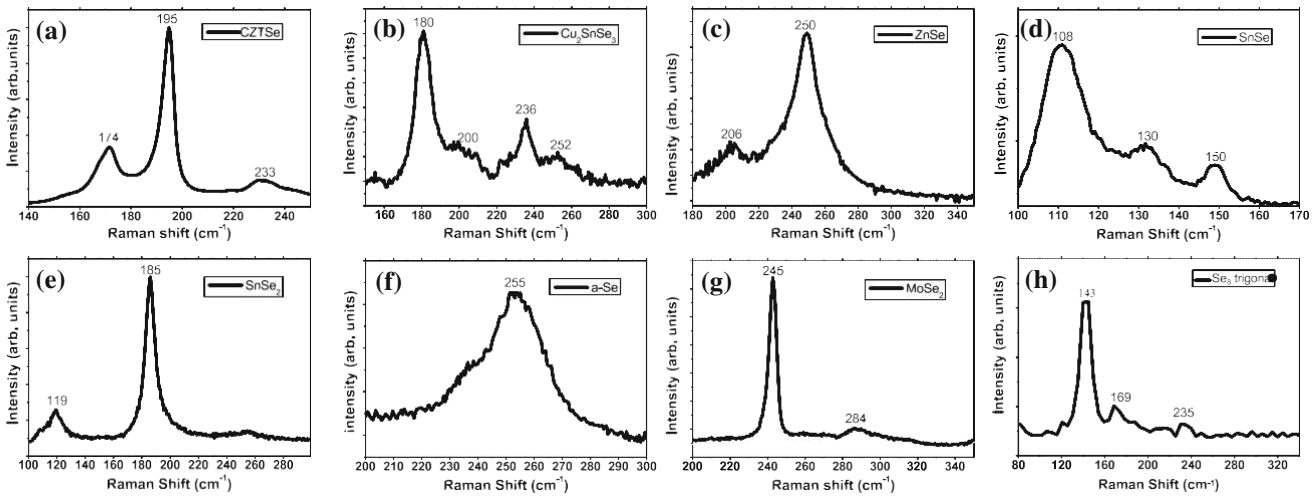

Fig. 1 RS spectra for different reference compounds. The excitation laser wavelength was 488 nm. The Raman shift for the dominant peaks in each spectrum are identified

Table 3 Experimental Raman frequency for several Se-based compounds, as shown in Fig. 1

Compound	Structure	Raman shift ðcm^{-1}Þ	Supporting references
CZTSe	Kesterite/ stannite	174, 195, 233	[47, 62, 79–81]
Cu_2SnSe_3	Cubic	180, 200, 236, 252	[55, 79]
ZnSe	Zinc blende	206, 250	[82]
SnSe	Orthorhombic	33, 71, 108, 130, 150	[74, 83]
$SnSe_2$	Hexagonal	119, 185	[74, 84, 85]
a-Se	Amorphous	255	[78]
$MoSe_2$	Hexagonal	245, 284	[86]
$Cu_{2-x}Se$	Cubic/ hexagonal	91, 260–270	[87]
Se_8	Trigonal	143, 237	[78]

reference just based on the literature for all crystalline phases is difficult due to several effects [94]: (1) the positions of the Raman peaks in a particular spectrum should be compared always with the value of a particular phonon mode of a reference sample, in our case, the value of 521.0 cm^{-1} for the position of the Raman peak corresponding to the TO phonon mode in a Si bulk crystal; in the literature, the value of this phonon is not unique [95] which can lead to different calibrations; (2) intrinsic properties of the samples such as strain [96], grain size [97, 98], temperature at what the measurements are made [81] and crystal quality will shift accordingly the Raman peaks and (3) the local temperature will also shift the peak; the evaluation of this temperature requires the measurement of the Raman peaks in Stokes and anti-Stokes regions which is not commonly performed if the objective of the measurement is the identification of crystalline phases. Thus, the positions of the Raman peaks measured by different research groups can differ by more than 1 cm^{-1}. For instance, the main peak of CZTSe, is presented here at 195 cm^{-1}, but it has been seen at the range 194–197 cm^{-1} [47, 62, 79, 80]. In addition to this, it has been theoretically predicted that comparing CZTSe with the kesterite structure to the stannite one should have differences in the peaks' positions in the range 2–4 cm^{-1} [90]. It can be said that for CZTS, Valakh et al. [99] were able to determine if a disordered kesterite structure coexists with a kesterite structure using Raman by deconvolution of CZTS peaks into separate peaks associated with the kesterite and stannite structures but so far, this analysis has not been performed for CZTSe.

Estimation of Raman's effective analysis depth in CZTSe

A central question in the use of RS for phase identification is the origin of the Raman signal due to a finite penetration depth of the laser radiation, which is dependent on the wavelength used. For this discussion, the knowledge of the absorption coefficient (a) is fundamental. Several reports on the CZTSe coefficient of absorption can be found in the literature with very different values [58, 100, 101]. We believe that some of these reports have been influenced by secondary phases and therefore, instead of taking values from the literature, we decided to measure the absorption coefficient of a sample prepared by us, for which all measurements shown in this work confirmed to be single-phase CZTSe. The thickness is 1500 nm with ½Cu]=ð½Zn]þ ½Sn]Þ ¼ 0:9 and ½Zn]=½Sn] ¼ 1:1. The sample was grown directly on SLG to allow the measurement of

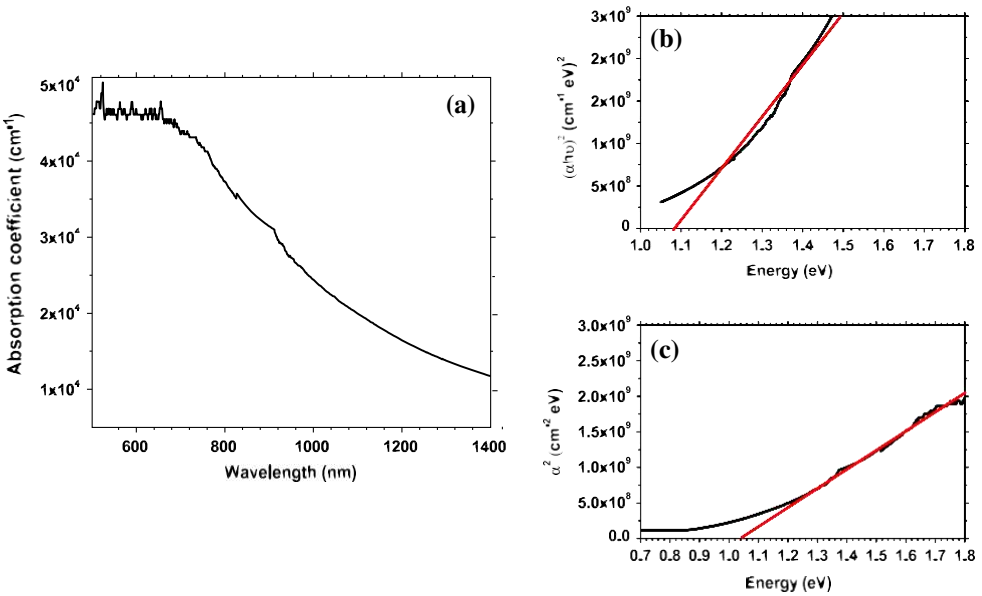

Fig. 2 a Absorption coefficient for CZTSe thin films grown on SLG. Bandgap energy estimation for CZTSe b using Tauc's method $(\alpha h\nu)^2$ versus $h\nu$; c using α^2 versus $h\nu$. The *red lines* are the extrapolation for the estimation of the bandgap energy (Color figure online)

transmittance. The absorption coefficient is calculated from transmittance (T) and reflectance (R) measurements using Eq. 1 [102]:

$$\alpha = -\frac{1}{d}\ln\left(\frac{\sqrt{(1-R)^4 + 4T^2R^2} - (1-R)^2}{2TR^2}\right); \quad (1)$$

where d is the thickness of the sample. For a direct bandgap semiconductor, Eq. 2 holds [102]:

$$\alpha = A(h\nu - E_{gap})^{1/2}; \quad (2)$$

where A is a constant, h is the Plank's constant, ν is the radiation frequency and E_{gap} is the bandgap energy. The absorption coefficient is shown in Fig. 2a and is higher than $4{:}5 \times 10^4$ cm^{-1} for wavelength values lower than 600 nm. One can estimate the bandgap energy using the conventional Tauc's method, which is based on the linear fit of $(h\nu \cdot \alpha)^2$ versus $h\nu$, [103] or by using a linear fit of α^2 versus $h\nu$ [102]. The two methods are presented in Fig. 2b, c, respectively, and give bandgap energy values of 1.08 and 1.05 eV. For both, the estimated error is 0.08 eV and comes mostly from the energy region where the fit is done. The second method is intrinsically easier to be implemented since the region of interest, i.e. the band edge, is more clearly identified. Also, that method provides values closer to the ones in the literature [62].

Having estimated the absorption coefficient, one can now calculate the Raman effective analysis depth (d_a) for different excitation. For the back-scattering configuration [28], which is the most common setup, $d_a = 1/(2\alpha)$, where 2 comes from the fact that the measured light has to penetrate the material, scatter and return to the surface. In essence, this value is a rough estimation of the thickness

Table 4 Estimated values for the Raman's effective analysis depth and laser penetration depth for PL measurements with different excitation in CZTSe

Wavelength (nm)	Absorption coefficient (cm^{-1})	Raman effective analysis depth (nm)	Laser penetration depth for PL (nm)
488	47287	106	212
514	46331	108	216
633	45727	109	218
785	38253	131	262
1035	22828	219	438

that one probes when performing RS on CZTSe films. The estimated values for the Raman effective analysis depth are shown in Table 4 and the effect of the wavelength in the scrutinized depth of the CZTS layer is schematically illustrated in Fig. 3. The numbers presented in the Table reveal what is, perhaps, the biggest limitation of this technique: for all of the excitation wavelengths shown and which are commonly accessible, the maximum thickness that one can probe is less than 200 nm. Higher excitation wavelength values would increase the thickness being probed but it makes the technique harder to be used due to the complexity of focusing, capturing the Raman signal in the infrared and the lower efficiency of RS too far from resonance conditions. In order to compensate for the small value of probing thickness, one could remove material from the surface by etching, sputtering [104] or other methods and performs the analysis at different depths, but this approach requires complex procedures or dedicated tools. Other possible solutions could be changing the focus

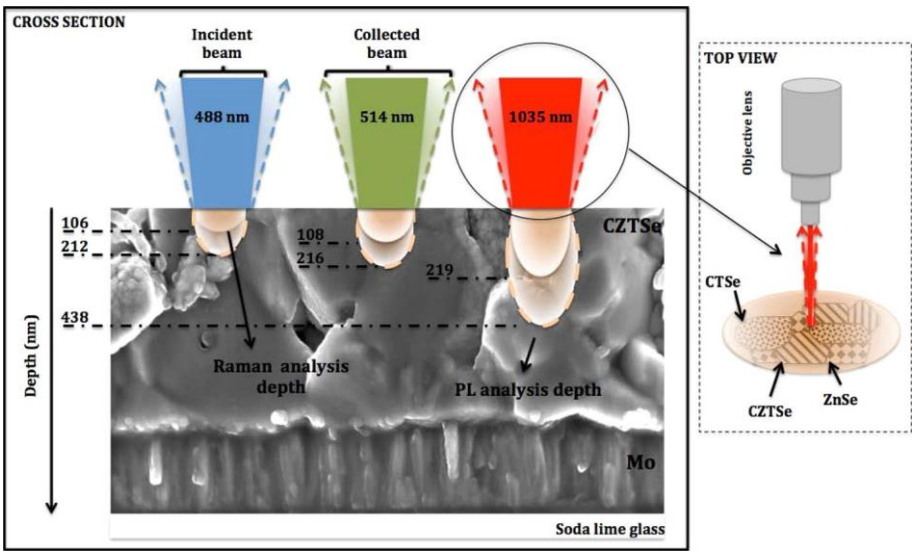

Fig. 3 Scheme of the Raman and PL's effective analysis depths for the laser wavelengths of 488, 514 and 1035 nm (Color figure online)

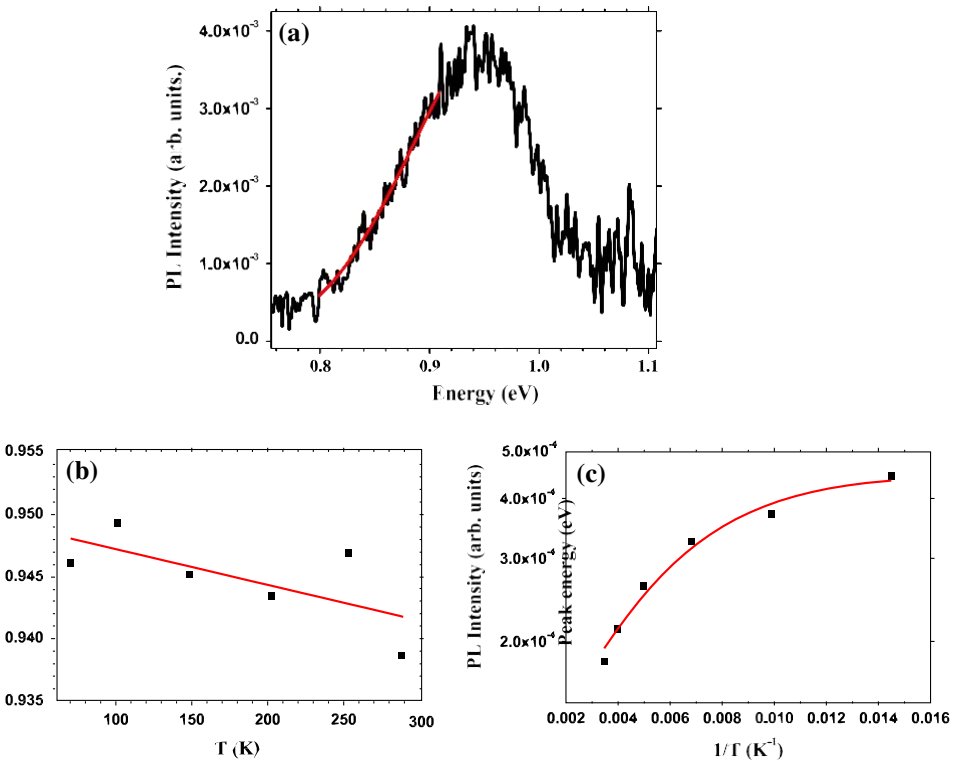

Fig. 4 a PL spectrum of CTZSe at 70 K. The low-energy side of the broad band was fitted with Eq. 4. b and c show the dependence on the temperature of the peak energy and PL intensity, respectively. In b, a linear fit was performed in order to describe the average shift of the data. In c, the experimental points were fitted with Eq. 3 (Color figure online)

point of the excitation laser [105] or perform the measurement in the cross section or from the back part of the film [106]. Increasing the intensity of the excitation laser would make more photons to arrive at deeper thicknesses but the limitation is still there since absorption follows an exponential behaviour and most of the signal would still be from the top part of the layer. Some of the mentioned techniques have already been applied to CZTS [93, 107], but are still to be used with CZTSe.

Photoluminescence studies

PL evaluates the electronic level structure of the crystalline phase present in the sample and gives additional contributions to the discussion of occurrence of secondary phases, namely if the estimation of the bandgap energy is possible. Comparatively to RS, PL investigates a layer with double the thickness for the same wavelength (see Table 4), thus giving information from a greater depth in the

sample [108]. Figure 4a depicts the PL spectrum measured at 70 K for the sample in which XRD and RS identified the presence of just the CZTSe phase. The emission is a broad asymmetric band in the range ""0.75–1.10 eV and centred at ""0.94 eV. This shape of the emission was reported previously in chalcogenide semiconductors [109, 110] and CZTSe mono-grains [111], and it is characteristic of electronic transitions occurring in semiconductors with high concentrations of ionized defects. These defects form random clusters of donors or acceptors which then lead to electrostatic potential fluctuations and are responsible for the appearance of densities of states' tails of the valence and conduction bands in the bandgap [112].

In order to discuss the origin of the radiative transitions observed in the sample, we studied the temperature dependence of the PL intensity. In spite of the low signal-to-noise ratio of the observed emission, as the temperature is increased from 70 to 288 K, we observed a red shift of 6.2 meV according to the linear fit to the experimental points shown in Fig. 4b. This shift is compatible with the potential fluctuations model mentioned previously [112, 113]. On the other hand, as the temperature was raised, we observed a decrease in the integrated PL intensity as a consequence of the thermal activation of non-radiative de-excitation channels. The experimental points in Fig. 4c are described by the equation for the temperature dependence of the PL intensity [114]:

$$I(T) = I_0 \left(1 + c_1 \exp\left(-\frac{E_1}{kT}\right)\right)^{-1}; \qquad (3)$$

where I_0 is the PL intensity at 0 K, c_1 is a parameter proportional to the ratio between the degeneracy of an hypothetical discrete high energy level and the radiative one, and E_1 is the energy difference between the two energy levels. Eq. 3 describes the thermal activation of a non-radiative recombination channel involving this discrete excited energy level. The fit is shown in Fig. 4c and the fitting parameters are $I_0 = 0{:}00045 \pm 0{:}00003$, $c_1 = 4 \pm 1$ and $E_1 = 29 \pm 6$ meV. This activation energy is lower than the energy needed to remove the carrier to the corresponding band [114]. Additionally, the low signal-to-noise ratio of the observed emission hindered the investigation of the excitation power dependence because the emission was measured with an excitation power of several tens of mW and with these high values of intensity, the temperature of the sample increases considerably.

In spite of the occurrence of potential wells on both bands, it is often the case that due to the difference of the effective masses of both charge carriers, the wells in the valence band are able to bind holes whereas the wells in the conduction bands do not bind electrons. Thus, the density of states of the valence band tail has a higher influence on the PL, contributing to the asymmetric shape of the emission. In fact, the intensity of the emission in the low-energy side ($I_{LE}(h\nu)$) of the emission follows the density of states of the valence band tail. The case of band-impurity type transitions, is given by [112]:

$$I_{LE}(h\nu) \propto \exp\left(-\frac{(E_g - E_I - h\nu)^2}{2\sigma^2}\right); \qquad (4)$$

where E_g is the band gap energy of the doped semiconductor, E_I is the binding energy of the hole to the acceptor level and σ describes the root mean square depth of the potential wells in the valence band. The fit of Eq. 4 to the range $0{:}80 \le E \le 0{:}91$ eV of the low-energy side of the emission band is shown in Fig. 4a and gives the values of $E_g - E_I = 0{:}973 \pm 0{:}012$ eV and $\sigma = 0{:}088 \pm 0{:}004$ eV. In the literature, values in the range of 18–25 meV have been found for σ in CZTSe and in the range of 55–65 meV in CZTSSe (with different [S]/[Se] ratios) [80, 111, 115]. At this point, we must note that other dependencies of the intensity on the photon energy and σ, corresponding to different types of radiative transitions involving charge carriers on the tails of both bands, the bands itself or acceptor states were tested, but no other acceptable fit was obtained due to the absence of physical meaning for the fitted parameters. Thus, we assume that the observed band corresponds to radiative recombinations of an electron in the conduction band and a hole in acceptor states influenced by the tail states of the valence band. Our results are in accordance with previous reports that pointed to the existence of fluctuating potentials in kesterites and chalcopirites [109, 110, 115–118]. Electrical measurements should be performed in order to discuss further the potential fluctuations model.

The bandgap energy can be estimated taking into account the activation energy obtained from the fit of Eq. 4 in Fig. 4c or from the spectroscopic energy (0.946 eV) of the maximum of intensity of the band. In the first case, E_g can be extracted if we know the binding energy of the hole to the radiative state, $E_g = E_I + 0{:}973$ eV. In the second case, assuming a band-impurity transition, the difference from the bandgap energy to the spectroscopic energy corresponds to the sum of E_I with the value of σ, $E_g - E_I = h\nu + \sigma$. In theory, we can calculate the binding energy of the hole from the dependence on the temperature of the PL intensity [114]. However, in our case, the only non-radiative de-excitation channel identified corresponds to the release of the hole to an excited discrete level and not to the valence band. Thus, the binding energy of the hole should be higher than the obtained activation energy (29 ± 6 meV) for that channel. In spite of that, the latter value allows us to calculate a lower limit for the bandgap energy: $E_g = 1{:}002$ and $E_g = 1{:}063$ eV from the fit of

Eq. 4 and from the spectroscopic energy, respectively. Both values are compatible with our estimates based on the absorption coefficient.

Our PL results show that just one emission band was observed and that band is compatible with the presence of just a single crystalline phase, the CZTSe one, in the scrutinized layer of the sample. From the list of secondary phases in Table 1, we see that for CTSe and SnSe phases, the bandgap energies are near the one of CZTSe which will locate the related PL approximately in the same spectroscopic region as for CZTSe. No evidence was obtained from our PL results for the presence of any other phases, which is in accordance with the results from the comparison of XRD with RS. Other reports in the literature [111, 119] show PL emissions with several bands which are created by the influence of secondary phases, so it can be said that PL is an experimental technique that gives an important contribution to the discussion of the crystalline phases.

Conclusions

In summary, we report a set of results that help identifying the presence of secondary phases in CZTSe thin films. We highlight the importance of using RS and PL as complementary phase-identification methods to XRD.

In the presented literature survey, we explained in detail why XRD can be used to identify the presence of CZTSe but not for the identification of all secondary phases, such as ZnSe or CTSe. Several unwanted compounds that might form during the growth of CZTSe were individually grown and studied using RS. All the compounds were grown using a two-step approach based on sputtering and selenization which is widely use for the growth of kesterites. All of the samples were characterized under the same conditions. The studied phases were CZTSe, ZnSe, CTSe, SnSe, $SnSe_2$, a-Se, $MoSe_2$ and $Cu_{2-x}Se$. We presented the spectrum of each phase and summarized all the identified peaks. The possible uncertainties about comparing peak positions were reduced due to the growth and characterization having been done in the same conditions. None of the phases have peaks which are superimposed upon the ones of CZTSe.

To further understand how useful RS can be, we have estimated the effective Raman analysis depth and concluded that what is effectively probed is the top 200 nm of the layer. The effective PL probing depth, also estimated, is twice the RS analysis depth for the same wavelength. The PL measurements revealed an asymmetric band compatible with the CZTSe phase and confirmed the value for the bandgap energy estimated from absorption measurements. The nature of the radiative and non-radiative recombination transitions was discussed considering the fluctuating potentials' model. Transitions of the type band-impurity were identified. The value of $c \approx 0{:}088 \pm 0{:}004$ eV was obtained for the root mean square depth of the potentials' wells in the valence band.

Acknowledgements The authors acknowledge the financial support of the following projects PTDC/CTM-MET-113486/2009, PEst-C/CT-M/LA0025/2011, RECI/FIS-NAN/0183/2012 (COMPETE: FCOMP-01-0124-FEDER-027494) from the Fundaç ao para a Ciência e Tecno-logia.

References

1. Wang W, Winkler MT, Gunawan O, Gokmen T, Todorov TK, Zhu Y, Mitzi DB (2013) Device characteristics of cztsse thin-film solar cells with 12.6 % efficiency. Adv Energy Mater 4(7). doi:10.1002/aenm.201301465
2. Shin B, Gunawan O, Zhu Y, Bojarczuk AN, Chey S, Guha S (2013) hin film solar cell with 8.4 power conversion efficiency using an earth-abundant Cu_2ZnSnS_4 absorber. Prog Photovolt Res Appl 21(1):72–76
3. IMEC-PressRelease-03/07/2013
4. Kato T, Hiroi H, Sakai N, Muraoka S, Sugimoto H (2012) Characterization of front and back interfaces on Cu_2ZnSnS_4 thin-film solar cells. In: 27th European photovoltaic solar energy conference and exhibition, pp 2236–2239
5. Tian Q, Xu XF, Han L, Tang M, Zou R, Chen Z, Muhuo Y, Yang J, Hu J (2012) Hydrophilic Cu_2ZnSnS_4 nanocrystals for printing flexible, low-cost and environmentally friendly solar cells. CrystEngComm 14:3847–3850
6. Guo L, Zhu Y, Gunawan O, Tayfun G, Deline VR, Ahmed S, Romankiw LT, Deligianni H (2014) Electrodeposited $Cu_2ZnSnSe_4$ thin film solar cell with 7 % power conversion efficiency. Prog Photovolt Res Appl 22(1):58–68
7. Hsu C-J, Duan H-S, Yang W, Zhou H, Yang Y (2013) Benign solutions and innovative sequential annealing processes for high performance $Cu_2ZnSn(Se,S)_4$ photovoltaics. Adv Energy Mater
8. Hsu W-C, Repins I, Beall C, DeHart C, To B, Yang W, Yang Y, Noufi R (2014) Growth mechanisms of co-evaporated kesterite: a comparison of Cu-rich and Zn-rich composition paths. Prog Photovolt Res Appl 22(1):35–43
9. Li JV, Kuciauskas D, Young MR, Repins IL (2013) Effects of sodium incorporation in co-evaporated $Cu_2ZnSnSe_4$ thin-film solar cells. Appl Phys Lett 102(16):163905
10. Li Y, Han Q, Kim TW, Shi W (2014) The optical influence of na on $Cu_2ZnSnSe_4$ films deposited with na-containing sol–gel precursor. J Sol–Gel Sci Technol 69(2):260–265
11. Li JV, Kuciauskas D, Young MR, Repins IL (2013) Erratum: effects of sodium incorporation in co-evaporated $Cu_2ZnSnSe_4$ thin-film solar cells [appl. phys. lett. 102, 163905 (2013)]. Appl Phy Lett 103(2):029901
12. Fella CM, Uhl AR, Romanyuk YE, Tiwari AN (2012) $Cu_2ZnSnSe_4$ absorbers processed from solution deposited metal salt precursors under different selenization conditions. Phys Status Solid A 209(6):1043–1048
13. Sarswat PK, Free ML (2014) Utility of by-product quantum dots obtained during synthesis of Cu_2ZnSnS_4 colloidal ink. Ceram Int 40(1A):859–869
14. Shavel A, Arbiol J, Cabot A (2010) Synthesis of quaternary chalcogenide nanocrystals: stannite Cu2Zn(x)Sn(y)Se(1? x?2y). J Am Chem Soc 132(13):4514–4515
15. Ford GM, Qijie G, Rakesh A, Hillhouse HW (2011) Earth abundant element $Cu_2Zn(Sn_{1-x}Ge_x)S_4$ nanocrystals for tunable

band gap solar cells: 6.8 % efficient device fabrication. Chem Mater 23(10):2626–2629
16. Haas W, Rath T, Pein A, Rattenberger J, Trimmel G, Hofer F (2011) The stoichiometry of single nanoparticles of copper zinc tin selenide. Chem Commun 47:2050–2052
17. Cao Y, Denny MS, Caspar JV, Farneth WE, Guo Q, Ionkin AS, Johnson LK, Lu M, Irina M, Radu D, Rosenfeld HD, Choudhury KR, Wu W (2012) High-efficiency solution-processed $Cu_2ZnSn(S,Se)_4$ thin-film solar cells prepared from binary and ternary nanoparticles. J Am Chem Soc 134(38):15644–15647
18. Du Y-F, Fan J-Q, Zhou W-H, Zhou Z-J, Jiao J, Wu S-X (2012) One-step synthesis of stoichiometric $Cu_2ZnSnSe_4$ as counter electrode for dye-sensitized solar cells. ACS Appl Mater Interfaces 4(3):1796–1802
19. Rath T, Haas W, Pein A, Saf R, Maier E, Kunert B, Hofer F, Resel R, Trimmel G (2012) Synthesis and characterization of copper zinc tin chalcogenide nanoparticles: influence of reactants on the chemical composition. Solar Energy Mater Solar Cells 101:87–94
20. Shi L, Li Q (2011) Thickness tunable $Cu_2ZnSnSe_4$ nanosheets. CrystEngComm 13:6507–6510
21. Wang K-C , Chen P, Tseng C-M (2013) Facile one-pot synthesis of Cu_2ZnSnS_4 quaternary nanoparticles using a microwave-assisted method. CrystEngComm 15:9863–9868
22. Miskin CK, Carter NJ, Yang W-C, Hages CJ, Stach E, Agrawal R (2013) High efficiency Cu_2ZnSnS_4 nanocrystal ink solar cells through improved nanoparticle synthesis and selenization. In: 2013 IEEE 39th photovoltaic specialists conference (PVSC), pp 0034–0037
23. Miskin CK, Yang W-C, Hages CJ, Carter NJ, Joglekar CS, Stach EA, Agrawal R (2014) 9.0 % efficient $Cu_2ZnSn(S,Se)_4$ solar cells from selenized nanoparticle inks. Prog Photovolt Res Appl
24. Wilman S, Shigeru I, Takashi H, Michio M (2013) Fabrication of $Cu_2ZnSnSe_4$ thin films from an electrodeposited Cu–Zn–Sn–Se/Cu–Sn–Se bilayer. Phys Status Solid C 10(7–8):1062–1066
25. Ikeda S, Septina W, Lin Yixin, Kyoraiseki A, Harada T, Matsumura M (2013) Electrochemical synthesis of Cu_2ZnSnS_4 and $Cu_2ZnSnSe_4$ thin films for solar cells. In: 2013 international renewable and sustainable energy conference (IRSEC), pp 1–4, March 2013
26. Altosaar M, Raudoja J, Timmo K, Danilson M, Grossberg M, Krustok J, Mellikov E (2008) $Cu_2Zn_{1-x}Cd_xSn(Se_{1-y}S_y)4$ solid solutions as absorber materials for solar cells. Phys Status Solid A 205(1):167–170
27. Fontané X, Calvo-Barrio L, Izquierdo-Roca V, Saucedo E, Pérez-Rodriguez A, Morante JR, Berg DM, Dale PJ, Siebentritt S (2011) In-depth resolved Raman scattering analysis for the identification of secondary phases: Characterization of Cu_2ZnSnS_4 layers for solar cell applications. Appl Phy Lett 98(18):181905
28. Fernandes PA, Salomé PMP, da Cunha AF (2011) Study of polycrystalline Cu_2ZnSnS_4 films by Raman scattering. J Alloys Compd 509(28):7600–7606
29. Ganchev M, Iljina J, Kaupmees L, Raadik T, Volobujeva O, Mere A, Altosaar M, Raudoja J, Mellikov E (2011) Phase composition of selenized $Cu_2ZnSnSe_4$ thin films determined by X-ray diffraction and raman spectroscopy. Thin Solid Films 519(21):7394–7398
30. Djemour R, Mousel M, Redinger A, Gtay L, Crossay A, Colombara D, Dale PJ, Susanne Siebentritt (2013) Detecting znse secondary phase in $Cu_2ZnSnSe_4$ by room temperature photoluminescence. Appl Phy Lett 102(22):222108
31. Colombara D, Robert EVC, Crossay A, Taylor A, Guennou M, Arasimowicz M, Malaquias JCB, Djemour R, Dale PJ (2014) Quantification of surface znse in $Cu_2ZnSnSe_4$-based solar cells by analysis of the spectral response. Solar Energy Mater Solar Cells 123:220–227
32. Bouaziz M, Boubaker K, Amlouk M, Belgacem S (2010) Effect of cu/sn concentration ratio on the phase equilibrium-related properties of Cu–Sn–S sprayed materials. J Phase Equilib Diffus 31(6):498–503
33. Redinger A, Berg DM, Dale PJ, Siebentritt S (2011) The consequences of kesterite equilibria for efficient solar cells. J Am Chem Soc 133(10):3320–3323
34. Tanaka T, Sueishi T, Saito K, Guo Q, Nishio M, Yu KM, Walukiewicz W (2012) Existence and removal of Cu_2Se second phase in coevaporated $Cu_2ZnSnSe_4$ thin films. J Appl Phys 111(5):053522
35. Fairbrother A, Garca-Hemme E, Izquierdo-Roca V, Fontan X, Pulgarn-Agudelo FA, Vigil-Galn O, Prez-Rodrguez A, Saucedo E (2012) Development of a selective chemical etch to improve the conversion efficiency of Zn-rich Cu_2ZnSnS_4 solar cells. J Am Chem Soc 134(19):8018–8021
36. Tsega M, Kuo D-H (2012) Defects and its effects on properties of Cu-deficient $Cu_2ZnSnSe_4$ bulks with different Zn/Sn ratios. Appl Phys Express 5(9):091201
37. Kaune G, Hartnauer S, Syrowatka F, Scheer R (2014) Phase formation in $Cu_2ZnSnSe_4$ thin films deposited with multi-stage co-evaporation processes. Solar Energy Mater Solar Cells, 120B:596–602
38. Kaune G, Hartnauer S, Scheer R (2014) In situ xrd investigation of $Cu_2ZnSnSe_4$ thin film growth by thermal co-evaporation. Phys Status Solid A. doi:10.1002/pssa.201330340
39. Tampo H, Makita K, Komaki H, Yamada A, Furue S, Ishizuka S, Shibata H, Matsubara K, Niki S (2014) Composition control of $Cu_2ZnSnSe_4$-based solar cells grown by coevaporation. Thin Solid Films 551:27–31
40. Fairbrother A, Fontan X, Izquierdo-Roca V, Placidi M, Sylla D, Espindola-Rodriguez M, Lpez-Mario S, Pulgarn FA, Vigil-Galn O, Prez-Rodrguez A, Saucedo E (2014) Secondary phase formation in Zn-rich $Cu_2ZnSnSe_4$-based solar cells annealed in low pressure and temperature conditions. Prog Photovolt Res Appl 22(4):479–487
41. Vora N, Blackburn J, Repins I, Beall C, To B, Pankow J, Teeter G, Young M, Noufi R (2012) Phase identification and control of thin films deposited by co-evaporation of elemental Cu, Zn, Sn, and Se. J Vac Sci Technol A 30(5):051201
42. Septina W, Ikeda S, Kyoraiseki A, Harada T, Matsumura M (2013) Single-step electrodeposition of a microcrystalline $Cu_2ZnSnSe_4$ thin film with a kesterite structure. Electrochim Acta 88:436–442
43. Siebentritt S (2013) Why are kesterite solar cells not 20 % efficient? Thin Solid Films 535:1–4
44. Larsen JK, Levent G, Siebentritt S (2011) Influence of secondary phase Cu_xSe on the optoelectronic quality of chalcopyrite thin films. Appl Phy Lett 98(20):201910
45. Wätjen JT, Engman J, Edoff M, Platzer-Björkman C (2012) Direct evidence of current blocking by znse in $Cu_2ZnSnSe_4$ solar cells. Appl Phy Lett 100(17):173510
46. Redinger A, Mousel M, Wolter MH, Valle N, Siebentritt S (2013) Influence of S/Se ratio on series resistance and on dominant recombination pathway in $Cu_2ZnSn(SSe)_4$ thin film solar cells. Thin Solid Films 535:291–295
47. Salomé PMP, Fernandes PA, da Cunha AF (2009) Morphological and structural characterization of $Cu_2ZnSnSe_4$ thin films grown by selenization of elemental precursor layers. Thin Solid Films 517(7):2531–2534
48. Hsu W-C, Repins I, Beall C, DeHart C, Teeter G, To B, Yang Y, Noufi R (2013) The effect of Zn excess on kesterite solar cells. Solar Energy Mater Solar Cells 113:160–164

49. Volobujeva O, Raudoja J, Mellikov E, Grossberg M, Bereznev S, Traksmaa R (2009) $Cu_2ZnSnSe_4$ films by selenization of SnZnCu sequential films. J Phys Chem Solids 70(3–4):567–570
50. Kim K-H, Amal I (2011) Growth of $Cu_2ZnSnSe_4$ thin films by selenization of sputtered single-layered Cu–Zn–Sn metallic precursors from a Cu–Zn–Sn alloy target. Electron Mater Lett 7(3):225–230
51. Repins I, Beall C, Vora N, DeHart C, Kuciauskas D, Dippo P, To B, Mann J, Hsu W-C, Goodrich A, Noufi R (2012) Co-evaporated $Cu_2ZnSnSe_4$ films and devices. Solar Energy Mater Solar Cells 101:154–159
52. Lund EA, Scarpulla MA (2013) Modeling Cu_2ZnSnS_4 (CZTS) solar cells with kesterite and stannite phase variation. Proc SPIE 8620:862015–862015-8
53. International Centre of Diffraction Data (ICDD) Datasheets: CZTSe: 04-010-6295; ZnSe: 04-007-4741; Cu_2SnSe_3: 03-065-4145; Cu_2Se: 01-071-4843; CuSe: 00-027-0185; SnSe: 04-004-4281; SnSe2: 01-089-3197; Mo: 04-001-2734
54. Schorr S (2007) Structural aspects of adamantine like multinary chalcogenides. Thin Solid Films 515(15):5985–5991
55. Ahmadi M, Pramana SS, Batabyal SK, Boothroyd C, Mhaisalkar SG, Lam YM (2013) Synthesis of Cu_2SnSe_3 nanocrystals for solution processable photovoltaic cells. Inorg Chem 52(4):1722–1728
56. Postnikov AV, Mortazavi Amiri NB (2013) Calculated vibration spectrum of monoclinic Cu_2SnSe_3 in comparison with kesterite-type $Cu_2ZnSnSe_4$. Phys Status Solid A 210(7):1332–1335.
57. Fan J, Carrillo-Cabrera W, Akselrud L, Antonyshyn I, Chen L, Grin Y (2013) New monoclinic phase at the composition Cu_2SnSe_3 and its thermoelectric properties. Inorg Chem 52(19):11067–11074
58. Wibowo RA, Kim WS, Lee ES, Munir B, Kim KH (2007) Single step preparation of quaternary thin films by RF magnetron sputtering from binary chalcogenide targets. J Phys Chem Solids 68(10):1908–1913
59. Suresh Babu G, Kishore Kumar YB, Uday Bhaskar P, Sundara Raja V (2008) Growth and characterization of co-evaporated $Cu_2ZnSnSe_4$ thin films for photovoltaic applications. J Phys D 41(20):205305
60. Zoppi G, Forbes I, Miles RW, Dale PJ, Scragg JJ, Peter LM (2009) $Cu_2ZnSnSe_4$ thin film solar cells produced by selenisation of magnetron sputtered precursors. Prog Photovolt Res Appl 17(5):315–319
61. Salomé PMP, Fernandes PA, da Cunha AF, Leitão JP, Malaquias J, Weber A, González JC, da Silva MIN (2010) Growth pressure dependence of $Cu_2ZnSnSe_4$ properties. Solar Energy Mater Solar Cells 94(12):2176–2180
62. Ahn SJ, Jung S, Gwak J, Cho A, Shin K, Yoon K, Park D, Cheong H, Jae HY (2010) Determination of band gap energy (E_g) of $Cu_2ZnSnSe_4$ thin films: on the discrepancies of reported band gap values. Appl Phy Lett 97(2):021905
63. Salomé PMP (2011) Chalcogenide thin films for solar cells: growth and properties. PhD thesis, Universidade de Aveiro, 2011.
64. Gao F, Yamazoe S, Maeda T, Nakanishi K, Wada T (2012) Structural and optical properties of in-free $Cu_2ZnSn(S,Se)_4$ solar cell materials. Jpn J Appl Phys 51(10S):10NC29
65. Wibowo RA, Jung WH, Kim KH (2010) Synthesis of $Cu_2ZnSnSe_4$ compound powders by solid state reaction using elemental powders. J Phys Chem Solids 71(12):1702–1706
66. Dong Y, Wang H, Nolas GS (2014) Synthesis and thermoelectric properties of cu excess $Cu_2ZnSnSe_4$. Phys Status Solid (RRL) 8(1):61–64.
67. Larach S, Shrader RE, Stocker CF (1957) Anomalous variation of band gap with composition in zinc sulfo- and seleno-tellurides. Phys Rev 108:587–589
68. Delgado GE, Mora AJ, Marcano G, Rincn C (2003) Crystal structure refinement of the semiconducting compound Cu_2SnSe_3 from X-ray powder diffraction data. Mater Res Bull 38(15):1949–1955
69. Marcano G, Rincon C, de Chalbaud LM, Bracho DB, Sanchez Perez G (2001) Crystal growth and structure, electrical, and optical characterization of the semiconductor Cu_2SnSe_3. J Appl Phys 90(4):1847–1853
70. Suresh Babu G, Kishore Kumar YB, Kumar Reddy Bharath Y, Sundara Raja V (2006) Growth and characterization of Cu_2SnSe_3 thin films. Mater Chem Phys 96(23):442–446
71. Haram Santosh K, Santhanam KSV (1995) Photoelectrochemical responses of orthorhombic and cubic copper selenides. J Electroanal Chem 396(12):63–68
72. Pathan HM, Lokhande CD, Amalnerkar DP, Seth T (2003) Modified chemical deposition and physico-chemical properties of copper(i) selenide thin films. Appl Surf Sci 211(1–4):48–56
73. Pathinettam Padiyan D, Marikani A, Murali KR (2000) Electrical and photoelectrical properties of vacuum deposited snse thin films. Cryst Res Technol 35(8):949–957
74. Fernandes PA, Sousa MG, Salomé PMP, Leitão JP, da Cunha AF (2013) Thermodynamic pathway for the formation of SnSe and $SnSe_2$ polycrystalline thin films by selenization of metal precursors. CrystEngComm 15:10278–10286
75. Bordas J, Robertson J, Jakobsson A (1978) Ultraviolet properties and band structure of SnS_2, $SnSe_2$, CdI_2, PbI_2, BiI_3 and BiOI crystals. J Phys C 11(12):2607
76. Salomé PMP, Fernandes PA, da Cunha AF (2010) Influence of selenization pressure on the growth of $Cu_2ZnSnSe_4$ films from stacked metallic layers. Phys Status Solid C 7(3–4):913–916
77. Salomé PMP, Malaquias J, Fernandes PA, da Cunha AF (2010) Mo bilayer for thin film photovoltaics revisited. J Phys D 43(34):345501
78. Kalugin VV, Minaev VS, Timoshenkov SP (2005) Structural and phase transformations in condensed selenium. J Optoelectron Adv Mater 7(4):1717–1741
79. Altosaar M, Raudoja J, Timmo K, Danilson M, Grossberg M, Krustok J, Mellikov E (2008) $Cu_2Zn_{1-x}Cd_xSn(Se_{1-y}S_y)_4$ solid solutions as absorber materials for solar cells. Phys Status Solid A 205(1):167–170.
80. Grossberg M, Krustok J, Raudoja J, Timmo K, Altosaar M, Raadik T (2011) Photoluminescence and raman study of $Cu_2ZnSn(Se_xS_{1-x})_4$ monograins for photovoltaic applications. Thin Solid Films 519(21):7403–7406
81. Sarswat PK, Free ML, Tiwari A (2011) Temperature-dependent study of the raman a mode of Cu_2ZnSnS_4 thin films. Phys Status Solid A 248(9):2170–2174
82. Lermann G, Bischof T, Materny A, Kiefer W, Kummell T, Bacher G, Forchel A, Landwehr G (1997) Resonant micro-raman investigations of the ZnSe–LO splitting in ii–vi semiconductor quantum wires. J Appl Phys 81(3):1446–1450
83. Chandrasekhar HR, Humphreys RG, Zwick U, Cardona M (1977) Infrared and raman spectra of the iv-vi compounds SnS and SnSe. Phys Rev B 15:2177–2183
84. Boscher Nicolas D, Carmalt Claire J, Palgrave Robert G, Parkin Ivan P (2008) Atmospheric pressure chemical vapour deposition of SnSe and $SnSe_2$ thin films on glass. Thin Solid Films 516(15):4750–4757
85. Walsh D, Jandl S, Harbec JY (1980) Raman active modes of the layer crystal $SnS_{2-x}Se_x$. J Phys C 13(7):L125
86. Sugai S, Ueda T (Dec 1982) High-pressure raman spectroscopy in the layered materials 2*h*-mos_2, 2*h*-$mose_2$, and 2*h*-$mote_2$. Phys Rev B 26:6554–6558
87. Xue C, Papadimitriou D, Raptis YS, Richter W, Esser N, Siebentritt S, Lux-Steiner MCh (2004) Micro-raman study of

orientation effects of Cu_xSe-crystallites on Cu-rich $CuGaSe_2$ thin films. J Appl Phys 96(4):1963–1966
88. Khare A, Himmetoglu B, Johnson M, Norris DJ, Cococcioni M, Aydil ES (2012) Calculation of the lattice dynamics and raman spectra of copper zinc tin chalcogenides and comparison to experiments. J Appl Phys 111(8):083707
89. Gürel T, Cem S, Çağın T (2011) Characterization of vibrational and mechanical properties of quaternary compounds Cu_2ZnSnS_4 and $Cu_2ZnSnSe_4$ in kesterite and stannite structures. Phys Rev B 84:205201
90. Beigom N, Amiri M, Postnikov, A (2010) Electronic structure and lattice dynamics in kesterite-type $Cu_2ZnSnSe_4$ from first-principles calculations. Phys Rev B 82:205204
91. Fernandes PA, Salomé PMP, da Cunha AF (2009) Growth and Raman scattering characterization of Cu_2ZnSnS_4 thin films. Thin Solid Films 517(7):2519–2523
92. Fernandes PA, Salomé PMP, Sartori AF, Malaquias J, da Cunha AF, Schubert B-A, González JC, Ribeiro GM (2013) Effects of sulphurization time on Cu_2ZnSnS_4 absorbers and thin films solar cells obtained from metallic precursors. Solar Energy Mater Solar Cells 115:157–165
93. Dimitrievska M, Fairbrother A, Fontan X, Jawhari T, Izquierdo-Roca V, Saucedo E, Prez-Rodrguez A (2014) Multiwavelength excitation Raman scattering study of polycrystalline kesterite Cu_2ZnSnS_4 thin films. Appl Phy Lett 104(2):021901
94. Gouadec G, Colomban P (2007) Raman spectroscopy of nanomaterials: how spectra relate to disorder, particle size and mechanical properties. Prog Cryst Growth Charact Mater 53(1):1–56
95. Lockwood DJ, Young JF (1991) Light scattering in semiconductor structures and superlattices, nato science series B, vol 273. Springer, Berlin
96. He J, Sun L, Zhang K, Wang W, Jiang J, Chen Y, Yang P, Chu J (2013) Effect of post-sulfurization on the composition, structure and optical properties of Cu_2ZnSnS_4 thin films deposited by sputtering from a single quaternary target. Appl Surf Sci 264:133–138
97. Sarswat Prashant K, Free Michael L (2013) An investigation of rapidly synthesized Cu_2ZnSnS_4 nanocrystals. J Cryst Growth 372:87–94
98. Khare A, Wills AW, Ammerman LM, Norris DJ, Aydil ES (2011) Size control and quantum confinement in Cu_2ZnSnS_4 nanocrystals. Chem Commun 47:11721–11723
99. Valakh MY, Kolomys OF, Ponomaryov SS, Yukhymchuk VO, Babichuk IS, Izquierdo-Roca V, Saucedo E, Perez-Rodriguez A, Morante JR, Schorr S, Bodnar IV (2013) Raman scattering and disorder effect in Cu_2ZnSnS_4. Phys Status Solid (RRL) 7(4):258–261
100. Li J, Ma T, Wei M, Liu W, Jiang G, Zhu C (2012) The $Cu_2ZnSnSe_4$ thin films solar cells synthesized by electrodeposition route. Appl Surf Sci 258(17):6261–6265
101. Shin SW, Kim IY, Hwan Jeong Chae, Ho Yun Jae, Yong Lee Jeong, Hyeok Kim Jin (2013) Band gap tunable and improved microstructure characteristics of $Cu_2ZnSn(S(1\text{-}x)Se(x))_4$ thin films by annealing under atmosphere containing S and Se. Curr Appl Phys 13(8):1837–1843
102. Caballero R, Guillén C (2003) Optical and electrical properties of $CuIn_{1-x}Ga_xSe_2$ thin films obtained by selenization of sequentially evaporated metallic layers. Thin Solid Films 431–432:200–204
103. Tauc J, Grigorovici R, Vancu A (1966) Optical properties and electronic structure of amorphous germanium. Phys Status Solid B 15(2):627–637
104. Fontane X, Izquierdo-Roca V, Calvo-Barrio L, Perez-Rodriguez A, Morante JR, Dominik Guettler, Eicke A, Tiwari AN (2009) Investigation of compositional inhomogeneities in complex polycrystalline $Cu(In,Ga)Se_2$ layers for solar cells. Appl Phy Lett 95(26):261912
105. Álvarez-García J, Pérez-Rodríguez A, Romano-Rodríguez A, Calvo-Barrio L, Barcones B, Morante JR, Siemer K, Luck I, Klenk R (2001) Microstructural characterisation of $CuInS_2$ polycrystalline films sulfurised by rapid thermal processing. Thin Solid Films 387(1–2):219–221
106. Calvo-Barrio L, Pérez-Rodríguez A, Álvarez-Garcia J, Romano-Rodríguez A, Barcones B, Morante JR, Siemer K, Luck I, Klenk R, Scheer R (2001) Combined in-depth scanning auger microscopy and Raman scattering characterisation of $CuInS_2$ polycrystalline films. Vacuum 63(1–2):315–321
107. Cheng A-J, Manno M, Khare A, Leighton C, Campbell SA, Aydil ES (2011) Imaging and phase identification of Cu_2ZnSnS_4 thin films using confocal raman spectroscopy. J Vac Sci Technol A 29(5):051203
108. Humlícek J (2000) Properties of silicon germanium and SiGe: carbon. INSPEC, The Institution of Electrical Engineers, London
109. Dirnstorfer I, Wagner MT, Hofmann DM, Lampert MD, Karg F, Meyer BK (1998) Characterization of $CuIn(Ga)Se_2$ thin films. Phys Status Solid A 168(1):163–175
110. Bauknecht A, Siebentritt S, Albert J, Lux-Steiner MCh (2001) Radiative recombination via intrinsic defects in $Cu_xGa_ySe_2$. J Appl Phys 89(8):4391–4400
111. Grossberg M, Krustok J, Timmo K, Altosaar M (2009) Radiative recombination in $Cu_2ZnSnSe_4$ monograins studied by photoluminescence spectroscopy. Thin Solid Films 517(7):2489–2492
112. Levanyuk AP, Osipov VV (1981) Edge luminescence of direct-gap semiconductors. Sov Phys Uspekhi 24(3):187
113. Leitão JP, Santos NM, Fernandes PA, Salomé PMP, da Cunha AF, González JC, Ribeiro GM, Matinaga FM (2011) Photoluminescence and electrical study of fluctuating potentials in Cu_2ZnSnS_4-based thin films. Phys Rev B 84:024120
114. Leitão JP, Carvalho A, Coutinho J, Pereira RN, Santos NM, Ankiewicz AO, Sobolev NA, Barroso M, Lundsgaard J (2011) Hansen, A. Nylandsted Larsen, and P. R. Briddon. Influence of ge content on the optical properties of X and W centers in dilute Si–Ge alloys. Phys Rev B 84(16):165211
115. Gokmen T, Gunawan O, Todorov TK, Mitzi DB (2013) Band tailing and efficiency limitation in kesterite solar cells. Appl Phy Lett 103(10):103506
116. Leitão JP, Santos NM, Fernandes PA, Salomé PMP, da Cunha AF, González JC, Matinaga FM (2011) Study of optical and structural properties of Cu_2ZnSnS_4 thin films. Thin Solid Films 519(21):7390–7393
117. Krustok J, Josepson R, Raadik T, Danilson M (2010) Potential fluctuations in $Cu_2ZnSnSe_4$ solar cells studied by temperature dependence of quantum efficiency curves. Phys B 405(15):3186–3189
118. Romero MJ, Du H, Teeter G, Yan Y, Al-Jassim MM (2011) Comparative study of the luminescence and intrinsic point defects in the kesterite Cu_2 $ZnSnS_4$ and chalcopyrite $Cu(In,Ga)Se_2$ thin films used in photovoltaic applications. Phys Rev B 84:165324
119. Redinger A, Hones K, Fontane X, Izquierdo-Roca V, Saucedo E, Valle N, Perez-Rodriguez A, Siebentritt S (2011) Detection of a ZnSe secondary phase in coevaporated $Cu_2ZnSnSe_4$ thin films. Appl Phy Lett 98(10):101907